

Reconstruction of Gamma-ray Direction using Boosted Decision Trees and the *Disp* Parameter

Sreela Das, 260772871 ✂

Master of Science

Department of Physics

McGill University

Montréal, Québec

July 10, 2019

A thesis submitted to McGill University in partial fulfillment of the
requirements of the degree of Master of Science

© Sreela Das, 2019

Acknowledgments

I would like to thank my supervisor, Prof. Kenneth Ragan for his guidance, advice and feedback for this work. I would also like to thank Tony Lin, for his work on the analysis package that enabled the work in this thesis. Thanks are also due to Prof. David Hanna, Benjamin Zitzer, Thomas Rosin, Matthew Lundy, Emma Ellingwood, Stephen O'Brien, and Sajan Kumar for their insights, discussions and constructive criticisms. Many thanks also to Paul Mercure and Juan Gallego for their technical assistance with the computer systems. Lastly, I would like to thank my family and friends for their love and support.

Abstract

The geometric reconstruction of shower direction at the VERITAS imaging atmospheric Cherenkov telescope system (IACTs) sees a substantial degradation at large zenith angles ($\phi > 45^\circ$). A machine-learning-based reconstruction of this direction is not expected to suffer from the same limitations because it does not rely on the geometry of the observation. In this work, we demonstrate the predicted efficiency of a reconstruction using boosted decision trees. We also test how well this translates to a data analysis by performing a proof of concept with compact and point-source objects.

nice!

Abrégé

La reconstruction géométrique de direction de cascades de particules au système d'imagerie télescopique Cherenkov (IACT) de VERITAS souffre d'une dégradation substantielle aux grands angles zénithiques ($\phi > 45^\circ$). Une reconstruction basée sur l'apprentissage machine ne devrait pas souffrir des mêmes limitations car elle ne compte pas sur la géométrie de l'observation. Dans ce travail, nous démontrons l'efficacité prévue d'une reconstruction à l'aide de Boosted Decision Trees optimisés. Nous testons également dans quelle mesure cela se traduit par une analyse de données en effectuant une validation de principe avec des objets compacts et à source ponctuelle.

Contents

Acknowledgments	i
Abstract	ii
Abrégé	iii
Contents	iv
List of Figures	vii
List of Tables	ix
1 Simulation and Analysis Packages	1
1.1 Direction Reconstruction	1
1.1.1 The <i>Disp</i> Method	1
1.2 Boosted Decision Trees	3
1.2.1 Training	3
1.2.2 Boosting	5
1.2.3 Testing	5
1.3 Noise in Simulations	6
2 Analysis Methods	7
2.1 Preliminary Test and Motivation	7
2.2 <i>Disp</i> Table and R_{68} Dependencies	8

2.2.1	Zenith Angle Dependence	8
2.2.2	Over-training	9
2.2.3	Noise Related Effects	12
2.2.4	Higher Statistics Tables	13
2.2.5	Acceptance Correction for Offset from Camera Center	13
2.2.6	Energy Dependence	16
2.3	R_{68} for Known Objects	19
2.3.1	R_{68} for the Crab Nebula	19
2.3.2	R_{68} for Mrk421	21
2.3.3	R_{68} for PKS1510-089	22
3	Conclusions	24
3.1	Summary	24
3.2	Discussion	25
3.3	Future Work	25
	Bibliography	26

List of Figures

1.1	Combining multiple telescopes in <i>Disp</i> reconstruction.	2
1.2	An example of a BDT	4
2.1	Crab direction reconstruction using Method0.	8
2.2	“standard” <i>Disp</i> table reconstruction.	9
2.3	Small <i>Disp</i> table reconstruction (noise = 250 MHz).	10
2.4	Over-training test.	11
2.5	<i>Disp</i> table reconstruction vs noise.	12
2.6	Higher statistics <i>Disp</i> table reconstruction vs noise.	14
2.7	Weight functions for offset from camera center.	15
2.8	R_{68} for the acceptance correction functions.	15
2.9	Energy Dependence of Method0. Colored bands are intended to guide the eye and do not represent data points.	16
2.10	Energy Dependence of the old Method5t. Colored bands are intended to guide the eye and do not represent data points.	17
2.11	Energy Dependence of the new Method5t. Colored bands intended to guide the eye and do not represent data points.	17
2.12	Energy and zenith dependence of the new Method5t.	18
2.13	Energy and zenith dependence of Method0 and the old Method5t	18
2.14	Performance of the new <i>Disp</i> method compared to Method0 and the old <i>Disp</i> method	19

2.15 Crab (horizon-to-horizon runs) direction reconstruction using Method5t. . .	20
2.16 Crab (LZA runs) direction reconstruction using Method5t.	21
2.17 Mrk421 direction reconstruction using Method5t.	22
2.18 PKS1510 direction reconstruction using Method5t.	23

List of Tables

OK, I assume there's some background
that goes in here?!

Chapter 1

Simulation and Analysis Packages

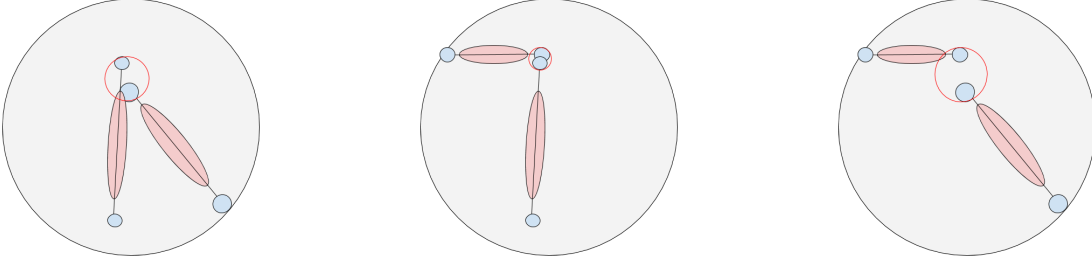
1.1 Direction Reconstruction

1.1.1 The *Disp* Method

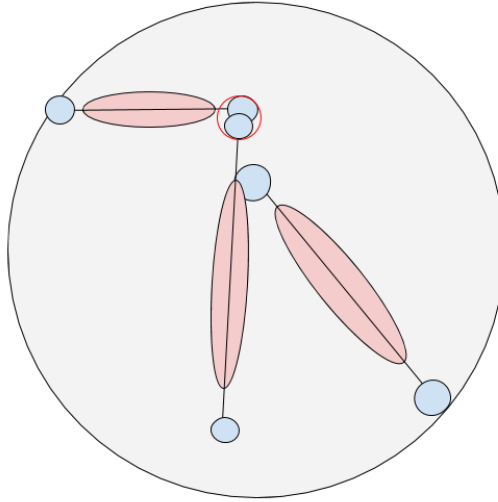
To compensate for this loss of predictive power, the *Disp method*, calculates the *Disp* parameter (quasi-analytically, using lookup tables and interpolating, or using **boosted decision trees**) for each individual telescope image to determine two potential locations for the arrival direction – along the major axis on either side of the weighted centroid of the image (see Fig. ??). This parameter is the (angular) vector displacement between the weighted centroid of the shower image and the estimated arrival direction of the initiating photon. In addition, the method also determines the two-dimensional uncertainty on this parameter which is expressed in terms of the radial (*DispError*) and angular (*MAError*) uncertainties. Together, these three parameters fully specify the direction of the initiating photon and the uncertainty on it, up to the head-tail ambiguity.

The method then compares this pair of coordinates (one at the head, and one at the

tail) for each pair of telescopes in the event reconstruction to find the pair of coordinates, one from either telescope, that are closest to each other (see Fig 1.1 for visual explanation). The weighted mean of this pair of coordinates is taken as the reconstructed shower direction, with the weights given by $DispError$ and $MAError$. The RMS distance of the two closest points (the points in the red circle in Fig. 1.1(d)) is taken to be the uncertainty on this position.



(a) First pair of telescopes in reconstruction, with the pair of closest coordinates. (b) Second pair of telescopes in reconstruction, with the pair of closest coordinates. (c) Third pair of telescopes in reconstruction, with the pair of closest coordinates.



(d) All telescopes in reconstruction, with the pair of closest coordinates from *all* pairs of telescopes.

Figure 1.1: Iterating through the unique pairs of telescopes, the closest coordinate pair is chosen, and the mean of those coordinates is taken as the direction of the initiating particle.

While using a quasi-analytic lookup table already provides substantial improvements on the LZA performance of the direction reconstruction, using boosted decision trees (BDTs) provides significantly better resolution comparable to (and in some regimes better than) that from the geometric reconstruction in the MZA range.

make
sure
this is
explained,
or use a
glossary?

1.2 Boosted Decision Trees

Decision trees use a predictive model, which maps parameters for an event to the value of the *Disp* parameter for the event. For example, Fig. 1.2 shows a decision tree that uses observed quantities to determine the temperature outside. The tree starts at the “root node”, which is the first test or question posed on the input data. The answer to this test determines the “branch” of the tree that is followed (in Fig. 1.2, Sunny or Overcast). Branches lead to “nodes,” which can either terminate (“leaf-nodes”), providing an answer, or pose a question and branch out again (“non-leaf nodes”) as demonstrated in Fig. 1.2.

The questions asked at each point are determined from a predictive model which may be based on analytic calculations (as in this example), or on Monte Carlo simulations (as in the case of this work). A basic algorithm for boosted decision tree (BDT) learning takes an input sample of data, generates a decision tree, uses a boosting algorithm to better discriminate mis-modeled inputs, and runs tests to provide some measures of its own performance. BDTs are especially robust for variables with non-linear correlations and have a fast application to data, relative to some other algorithms. This section contains a brief description of these individual steps.

1.2.1 Training

Decision trees are a type of supervised learning algorithm. This means the training data contains the input variables as well as the expected output variables. For our purposes,

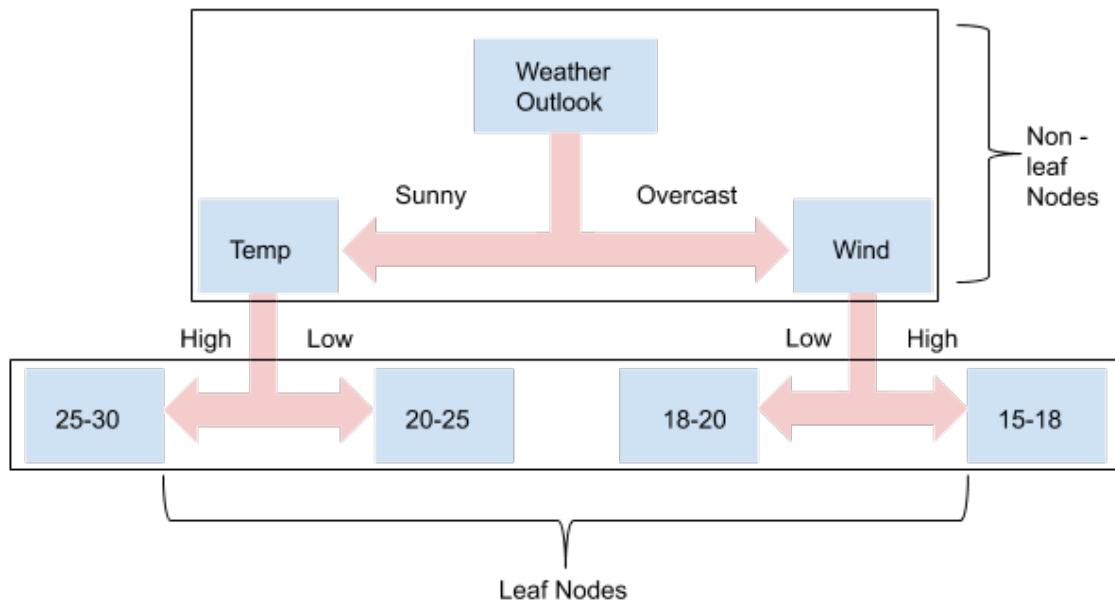


Figure 1.2: An example of a BDT to determine the temperature using observables. Each test or question is represented by a “node,” which creates two or more “branches” of the tree. Each of these branches represent a particular answer (or set of answers) to the test/question. The final results, where no test is performed is referred to as a leaf.

this means the algorithm is provided with a training sample comprised of the values of the parameters used for the reconstruction of each event along with the true value (from simulations) of the parameter to be reconstructed. The training process then generates correlation matrices for the dependent variables. With this information the algorithm is able to create a decision tree where each non-leaf node denotes a test on an attribute and each branch represents an outcome of the test, at each step using a test that best bifurcates the input data. In Fig.1.2 this can be represented by the fact that on an overcast day, the wind-speed is a strong discriminating factor, but on a sunny day wind is a smaller effect.

1.2.2 Boosting

To avoid having multiple identical trees, a higher weight is assigned to events that are canonically hard to discriminate. This means that within the training, more time is spent on discriminating between events that are hard to distinguish and this assigning of weights to preferentially train more on specific parts of parameter space is referred to as boosting.

1.2.3 Testing

The implementation of the *Disp* method in *VEGAS* (and *EventDisplay*) uses the ROOT Toolkit for Multi-Variate Analysis (TMVA) package. The TMVA package contains implementations of several complex algorithms including neural networks, Fisher discriminants and boosted decision trees (BDTs). The TMVA package contains a built-in testing step to measure certain parameters to help determine the goodness of the training. This step is used to measure deviations of the reconstruction of the testing data-set and the training data-set. A large difference between the performance on the training and testing sets could mean the method has been trained on noise in the training data-set rather than on relevant parameters. This misinterpretation of nuisance parameters or noise in the training sample as relevant effects is referred to as *overtraining*.

1.3 Noise in Simulations

On the other hand, NSB photons may "promote" subthreshold showers above our trigger threshold.

The night sky background (NSB) level is also a priori expected to influence the reconstruction efficiency for gamma rays. A higher level of NSB photons increases the threshold needed to remove background photons, thereby causing a greater loss of lower energy gamma rays. ~~(This decreases the sensitivity to lower energy photons and affects the gamma-ray effective area.)~~

Thus it is expected that the NSB needs to be modeled in our simulations.

To incorporate this effect in the simulations, gamma-ray shower simulations are created with multiple different noise levels. For the purposes of this work, simulations with noise levels of 200, 250, 300, 350, and 450 MHz were used.

While the units used for noise in this work are MHz, this frequency is not that of the background photons. Instead this represents the photon flux (which is measured in photo-electrons $\text{ns}^{-1} \text{m}^{-2} \text{sr}^{-1}$) folded in with ~~the~~ a number of instrument parameters that include mirror area (m^2), reflectivity (as %) and pixel size of the PMTs (rad). It tracks roughly the number of photo-electrons from the night sky background per pixel of the camera. ^{is} These values should accurately recreate the NSB levels at VERITAS observations.

range of

Chapter 2

Analysis Methods

2.1 Preliminary Test and Motivation

> The motivation for this work was to refine, understand, and document the *Disp* method of direction reconstruction. This method was expected to be useful to better resolve objects observed close to the horizon and facilitate studying the stability of the reconstruction to the zenith angle of observation. There was also the possibility of using machine learning algorithms to improve resolution beyond that of the standard geometric reconstruction. In particular, an improved angular resolution on the Crab ^{may} open up the possibility of resolving the ^{spatial} extension of the Crab Nebula with the VERITAS instrument. good!

> A preliminary test for this was enabled by a set of runs where the Crab was tracked from horizon to culmination and back to the horizon (from the nights of Jan 12 2018, Jan 13 2018, and Jan 04, 2019). This provided a reference data set with high significance to track ^{the} energy and zenith dependence of the direction reconstruction in stable (and therefore directly comparable) weather conditions. The differential resolution for the Crab data was measured in several energy and zenith bins and is presented in Fig. 2.1 ?

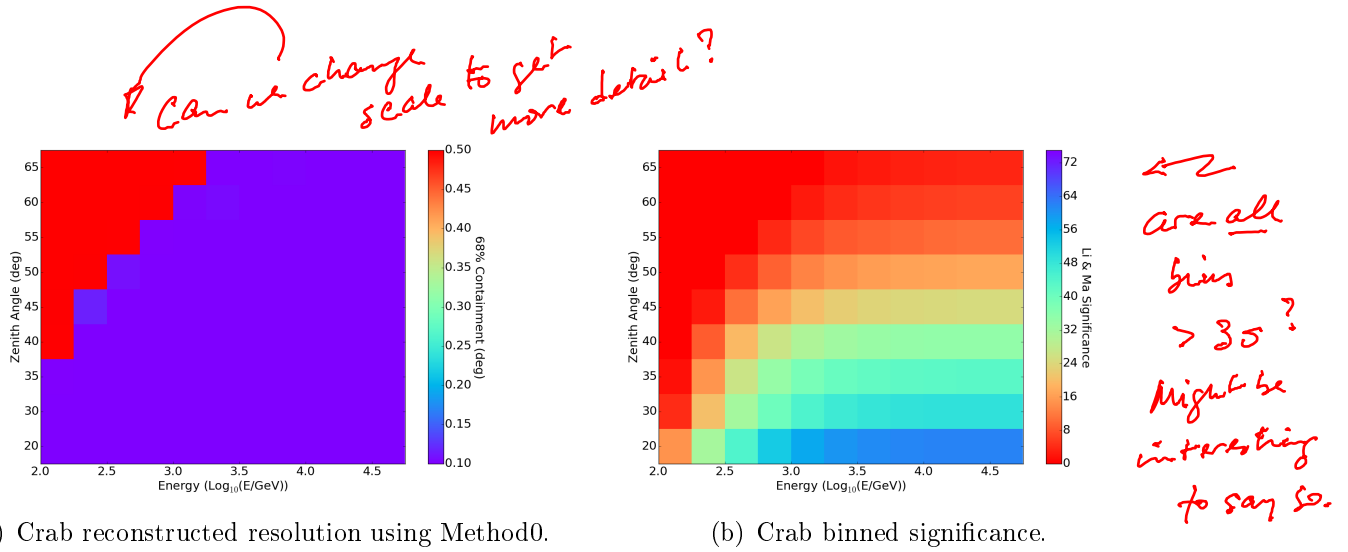


Figure 2.1: Reconstruction of the Crab direction using Method0 (standard geometric reconstruction from *VEGAS*).

2.2 *Disp* Table and R_{68} Dependencies

The BDT weight tables were generated independently of the old *Disp* method in order to have ^{1. a well understood} clear documentation of the underlying effects and dependencies. For the purposes of this work, the 68% containment radius in angular ^{position} offset (R_{68}) is used as a measure of angular resolution and performance of the reconstruction.

perhaps show one 2-D plot w/ log scale & fit?

2.2.1 Zenith Angle Dependence

A set of *Disp* tables was generated with a small sample of ^{simulation} events ($n \approx 1.9 \times 10^6$) across the range of zenith angles of interest ($20^\circ - 65^\circ$). This was compared to the regular *Disp* method. Since there was no record of the training sample size for the standard tables, this test sample was useful in determining the resolution of the *Disp* method with a relatively small computational footprint. Additionally, it allowed for some simple tests of dependence of the *Disp* tables on parameters not explicitly in the *Disp* tables.

~~This~~ small *Disp* tables and the standard *Disp* tables were used to reconstruct simulation events and compared with Method0 (the standard method of direction reconstruction). In both cases, the *Disp* method performs better than Method0 at the largest zenith angles ($\geq 55^\circ$, see 2.2-2.3 for R_{68} of the *Disp* methods divided by that for Method0 at the same zenith angle). From here it is clear that the regime of interest for the *Disp* method is $\geq 45^\circ$.

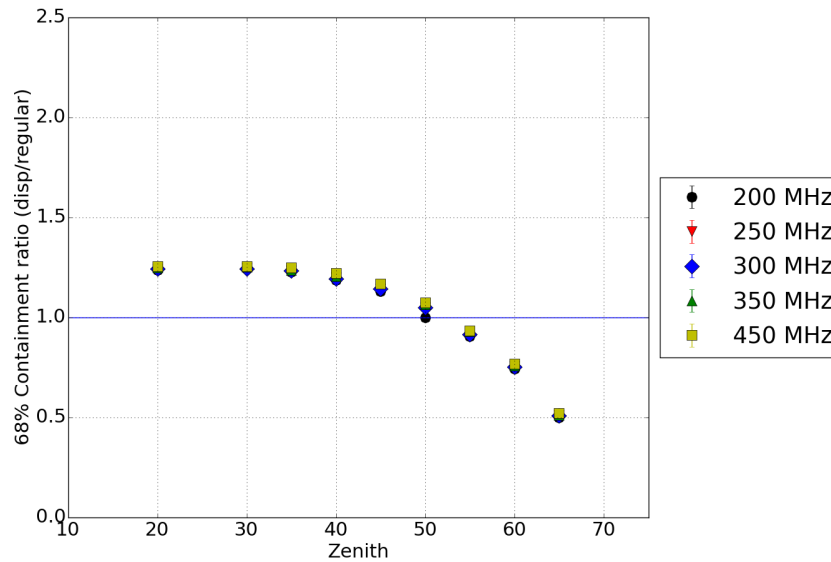


Figure 2.2: Ratio of R_{68} of the “standard” *Disp* table to that from Method0. Since this is the ratio of methods, the horizontal blue line denotes the performance using Method0; and this method performs better than Method0 for zenith $\geq 45^\circ$.

2.2.2 Over-training

BDT-based regression is quite robust under non-linear correlations between discriminating parameters, however the primary vulnerability of this method is that to over-training - where the decision tree starts to be informed by noise and nuisance parameters in the training sample rather than relevant effects. This results in substantially different reconstruction efficiencies between training and testing samples. The ROOT TMVA

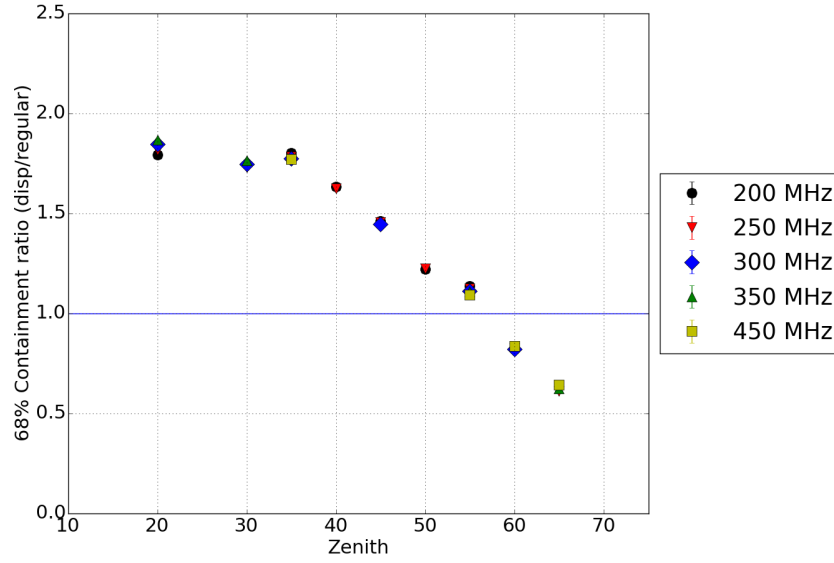
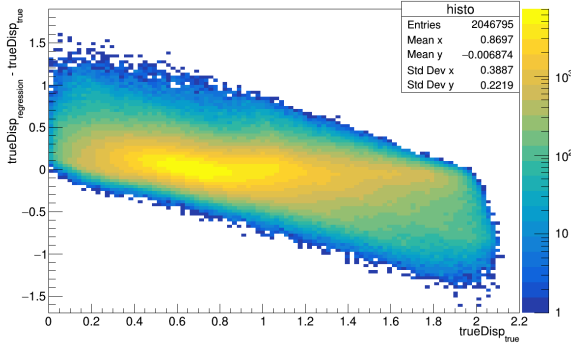


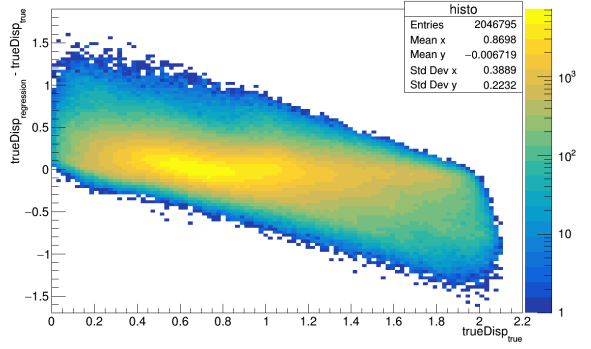
Figure 2.3: Ratio of the R_{68} from reconstruction using the small *Disp* table ($\sim 1.9 \times 10^6$ events all at noise = 250 MHz) and that from Method0. Note the horizontal blue line denotes the performance using Method0, so this method performs better than Method0 for zenith

> 45° . ^{~50} includes a package ~~has a built in~~ test for over-training where it randomly selects a given fraction of the supplied events (for the purposes of this work, this fraction was taken to be 50%) to use for testing. These events are then not used to train the regression trees and are instead used only to generate a measure of the over-training. This check of the over-training for one of the test tables (noise = 450 MHz), shown in Fig. 2.4, demonstrates that there was no meaningful over-training of the table, at least based on effects in the training sample.

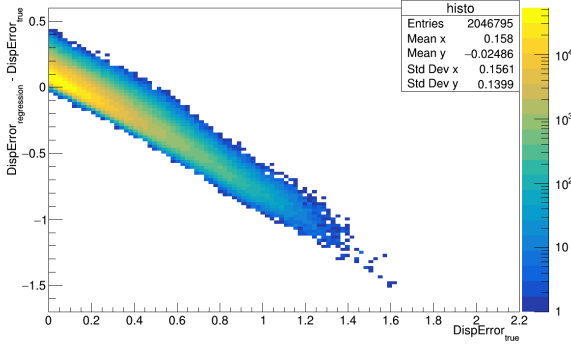
There remains however, the possibility of effects related to noise level that might appear in the training *and* testing samples (which are generated separately at each noise level), but not in observational data sets, which would be overlooked by this measure of over-training.



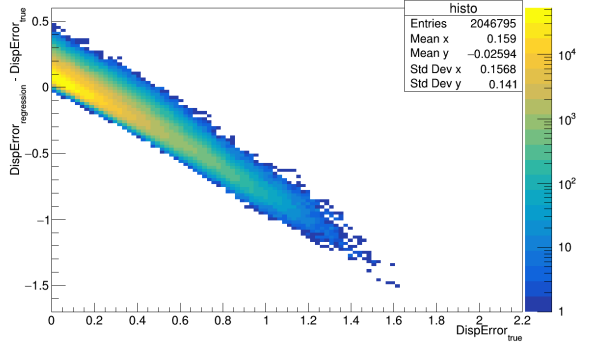
(a) Deviation of reconstructed *Disp* parameter from Monte-Carlo *Disp* parameter in training sample.



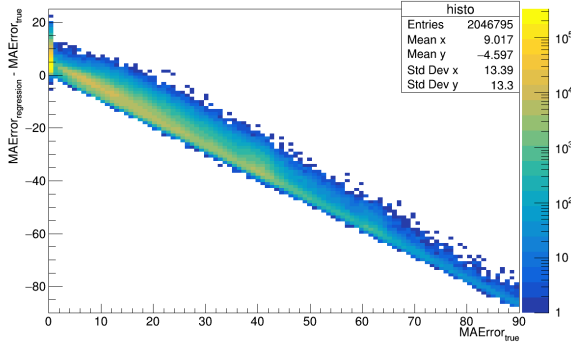
(b) Deviation of reconstructed *Disp* parameter from Monte-Carlo *Disp* parameter in testing sample.



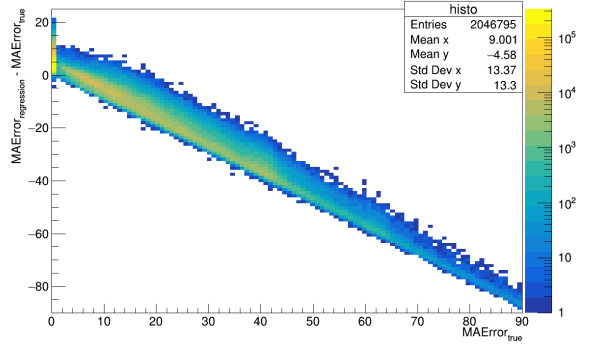
(c) Deviation of reconstructed *Disp* Error parameter from Monte-Carlo *Disp* Error parameter in training sample.



(d) Deviation of reconstructed *Disp* Error parameter from Monte-Carlo *Disp* Error parameter in testing sample.



(e) Deviation of reconstructed MAError parameter from Monte-Carlo MAError parameter in training sample.



(f) Deviation of reconstructed MAError parameter from Monte-Carlo MAError parameter in testing sample.

Figure 2.4: Over-training check on reconstruction using a *Disp* table generated at a single noise level. The left column shows the deviation of the reconstructed parameter from the true value in the training sample and the column on the right shows the same in the testing sample. The difference between the two columns is small which suggests there is little or no overtraining.

2.2.3 Noise Related Effects

The first set of *Disp* tables was also generated at a single noise level (250 MHz), allowing us to test the dependence of the resolution of this method (as measured by R_{68}) on noise level – some kind of noise-dependent effect would suggest over-training that would not be evident from the testing sample in the ROOT TMVA method since all the data provided to the package would have been at the same noise level. A comparison of angular resolution across noise levels revealed no significant dependence of the R_{68} on noise (see Fig. 2.2, 2.3 and 2.5).

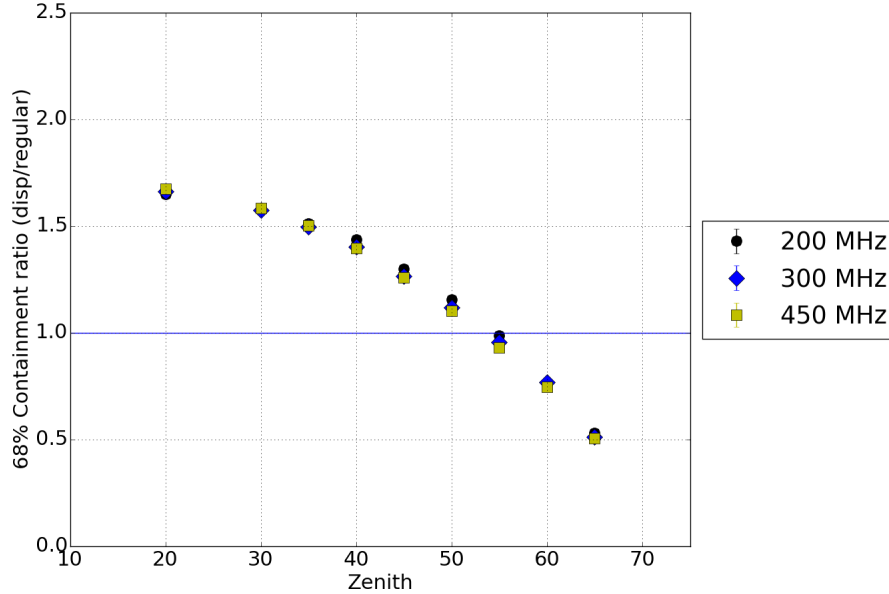


Figure 2.5: Ratio of R_{68} of the noise=450MHz *Disp* table ($\sim 2.1 \times 10^6$ events) to that from Method0. *Note that the result is largely independent of the noise level in the simulation sample.*

A second set of test *Disp* tables was generated using a single noise level (noise = 450 MHz) to test for noise-related over-training (see Fig. 2.5). These tables performed slightly better than the first test tables and comparably to the standard *Disp* tables. Since the noise-related effects did not seem to play a significant role in reconstruction, noise was dropped as a discriminating parameter for further analysis.

To generate a set of *Disp* tables with better angular resolution (as measured by R_{68}), another set of *Disp* tables was trained on a larger number of simulations across zenith angles (as before) as well as across the noise spectrum.

but you're just
concluded noise is
not relevant?

2.2.4 Higher Statistics Tables

Once it was determined that there was no significant over-training in the small sample *Disp* tables, and the noise level had little bearing on the R_{68} measure of the reconstruction, it was determined that different noise level simulation events could be used as independent training events to have a higher statistics *Disp* table, and make small improvements on the statistical uncertainty on the reconstruction. The simulation data from across the noise spectrum and zenith range was used to generate a *Disp* table that sampled the entire parameter space more exhaustively.

A new set of *Disp* tables was generated (Fig. 2.6) with a training sample four times that of the initial test tables. The improvements in resolution due to change in sample size were modest, and confined to the range of zenith angles (zenith $> 45^\circ$) where the standard method outperforms the *Disp* method quite considerably.

As expected from the small statistical uncertainty on the R_{68} values, this increase in sample size did not lead to any meaningful improvements and a training sample of $\sim 2 \times 10^6$ was determined to be sufficient to achieve the desired resolution with small uncertainties.

2.2.5 Acceptance Correction for Offset from Camera Center

Showers arriving further from the camera center have a larger fraction of the shower arriving outside of the camera and therefore being lost. These showers are therefore reconstructed with a lower efficiency and resolution than showers arriving closer to the

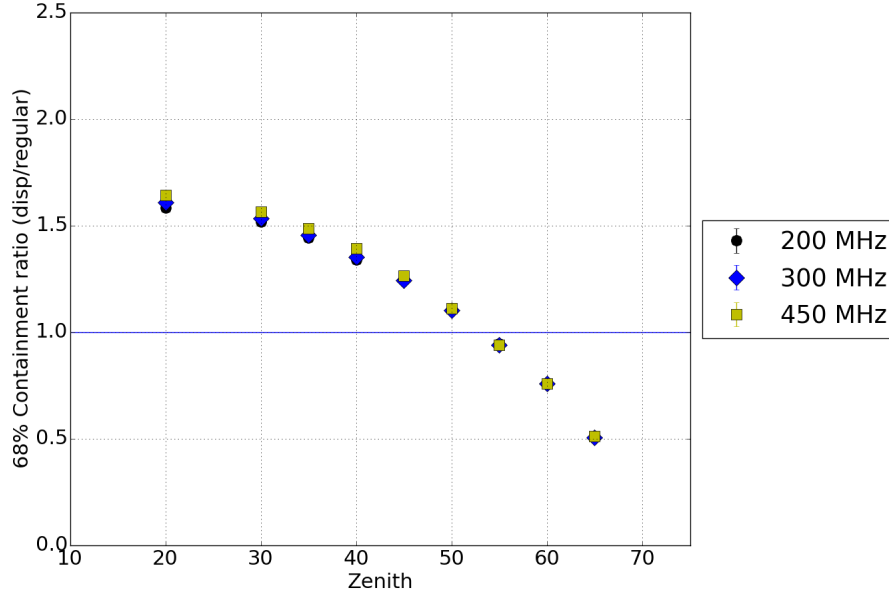


Figure 2.6: Ratio of R_{68} of the noise=450MHz *Disp* table ($\sim 8.4 \times 10^6$ events) to that from Method0 for a higher statistics *Disp* table.

camera center. To compensate for this in the BDT training, so that the training sample does not mis-characterize the overabundance of events closer to the camera center as an anisotropy in incoming gamma rays, we fold in an acceptance correction by assigning a larger weight to events that are further away from the camera center.

The acceptance correction used here affects the training sample and therefore might be assumed to affect the resolution in a zenith dependent way, ^{perhaps} explaining the difference in performance between the new *Disp* tables and the old ones. This was tested by using a number of different correction functions in the training sample, as shown in Fig. 2.7

These tests reveal small changes in the R_{68} value despite large changes in the correction function (Fig. 2.8). This suggests that the *Disp* tables are not sensitive to changes in acceptance and therefore the different acceptance functions are unlikely to be the reason why the new *Disp* tables perform worse at smaller zenith angles.

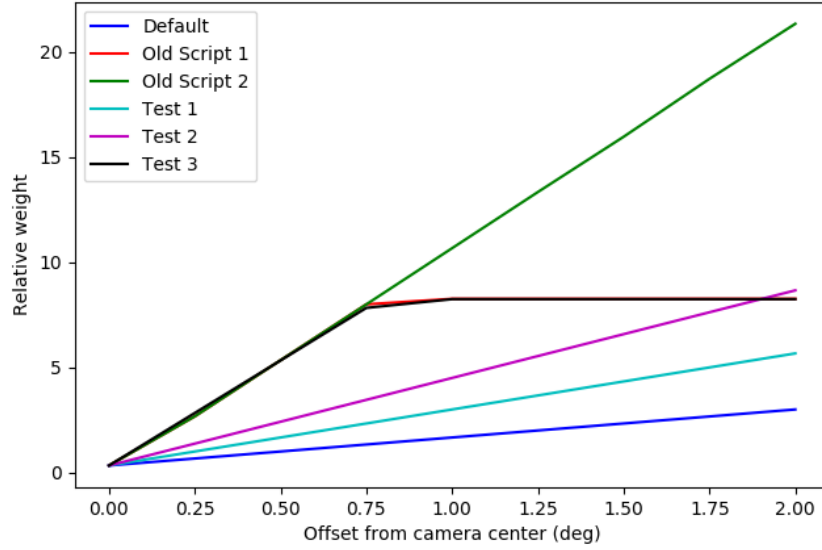


Figure 2.7: The weight functions used in the training samples in the new tables (Default, Test 1, Test 2 and Test 3) and those found in the scripts used to generate the older tables (Old Script 1, Old Script 2).

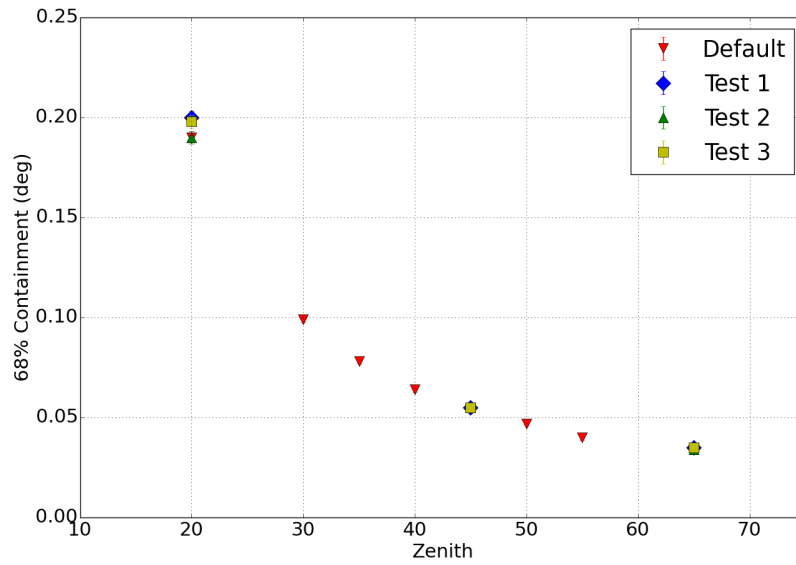
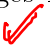
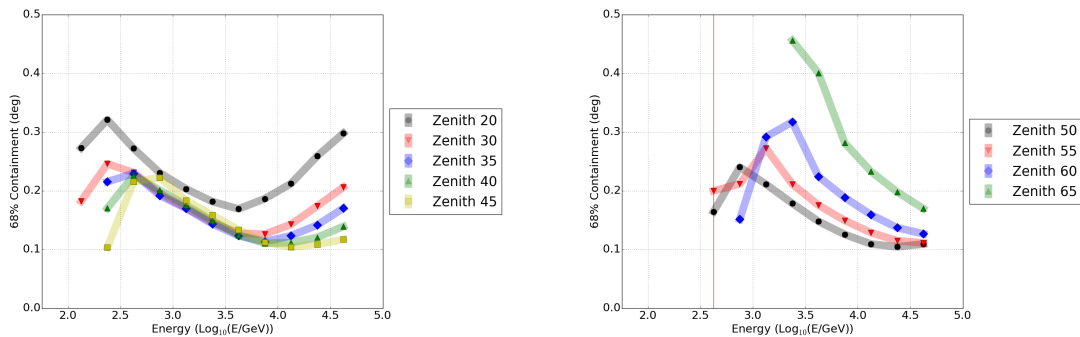


Figure 2.8: R_{68} for each acceptance correction function shown in Fig. 2.7. The changes in acceptance correction do not meaningfully change the R_{68} for the reconstruction. 

2.2.6 Energy Dependence

Another important dependence of the reconstruction resolution (and therefore the R_{68}) is that on energy. Higher energy photons are expected to comprise a large fraction of LZA photons ~~since they have to travel longer through the atmosphere and therefore must have higher energies to remain above the energy threshold.~~ *because lower energy showers ~~are~~ suffer more absorption in the atmosphere* Conversely, high energy photons make up a small fraction of SZA photons (and more generally, all cosmic photons) due to the $\sim E^{-2}$ shape of the spectrum. A better resolution at higher energy would also be expected to contribute to the improved resolution at LZA.



(a) Energy Dependence of Method0 at small and medium zenith angles. (b) Energy Dependence of Method0 at large zenith angles.

Figure 2.9: Energy Dependence of Method0. Colored bands are intended to guide the eye and do not represent data points.

The Method0 energy dependence (Fig. 2.9) follows the same trend as in Fig. ?? - *angles* seeing the best resolution for all zenith *or* angles in the 3-30 TeV range as well as a low energy improvement likely driven by high statistics. The energy dependence for the older *Disp* tables (Fig. 2.10) appears to have a minimum in R_{68} close to 1 TeV. These old *Disp* tables also see a degradation in resolution at the highest energies. The newer *Disp* tables (Fig. 2.11) on the other hand appear *✓* to do **better at higher energies for all zenith angles**. At energies above ~ 1 TeV and zenith angle greater than 30° , the R_{68} is at or better than 0.3° (see Fig. 2.12).

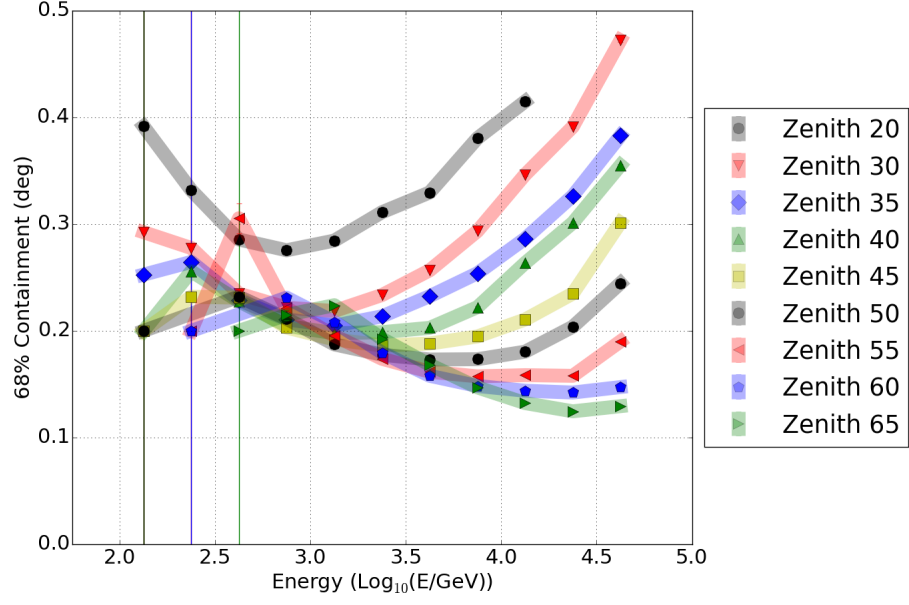


Figure 2.10: Energy Dependence of the old Method5t. Colored bands are intended to guide the eye and do not represent data points.

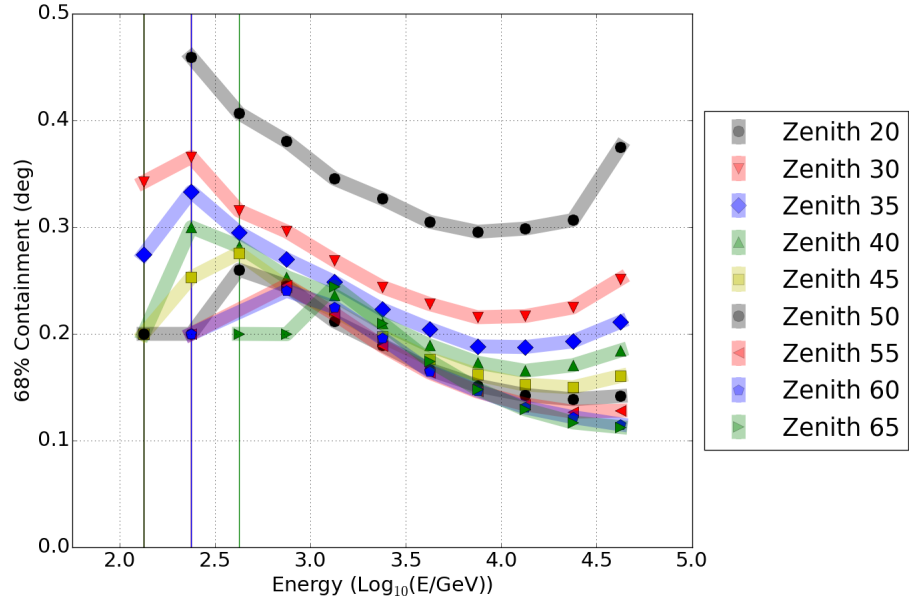


Figure 2.11: Energy Dependence of the new Method5t. Colored bands intended to guide the eye and do not represent data points.

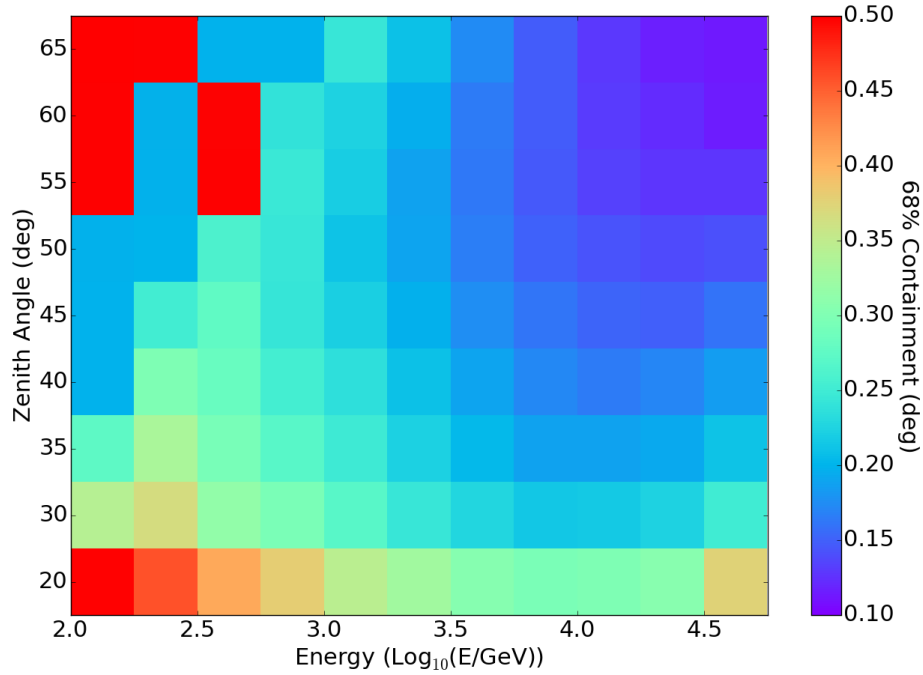


Figure 2.12: Energy and zenith dependence of the new Method5t, with colors denoting the R_{68} and red denoting $R_{68} \geq 0.60^\circ$. The upper-left corner shows regions of loss in resolution in the large-zenith low-energy region, ~~this is~~ due to low statistics.

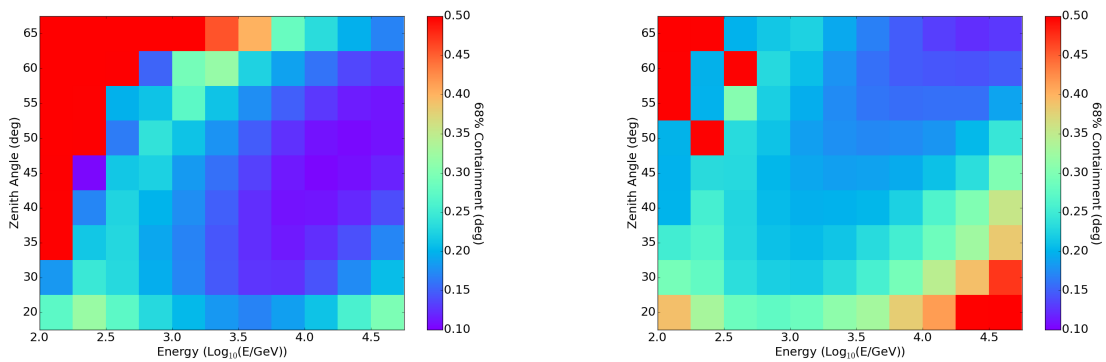


Figure 2.13: Energy and zenith dependence of the geometric reconstruction (left) and the old Method5t (right), with colors denoting the R_{68} and red denoting $R_{68} \geq 0.60^\circ$.

I don't think this is referenced in the text?

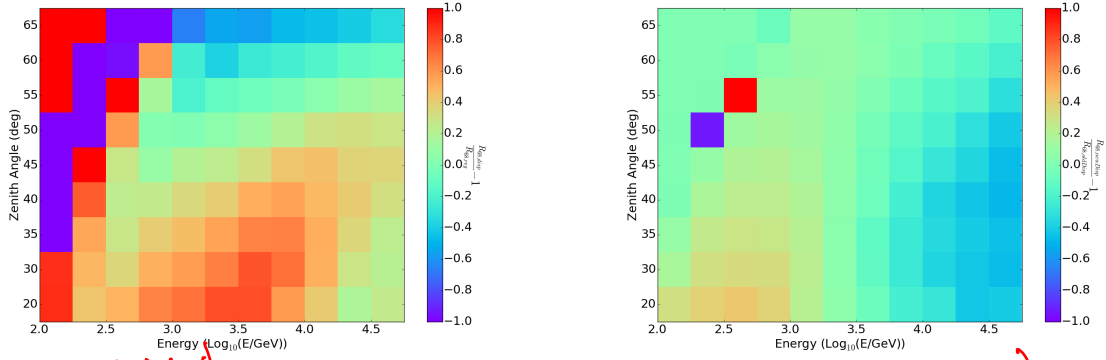


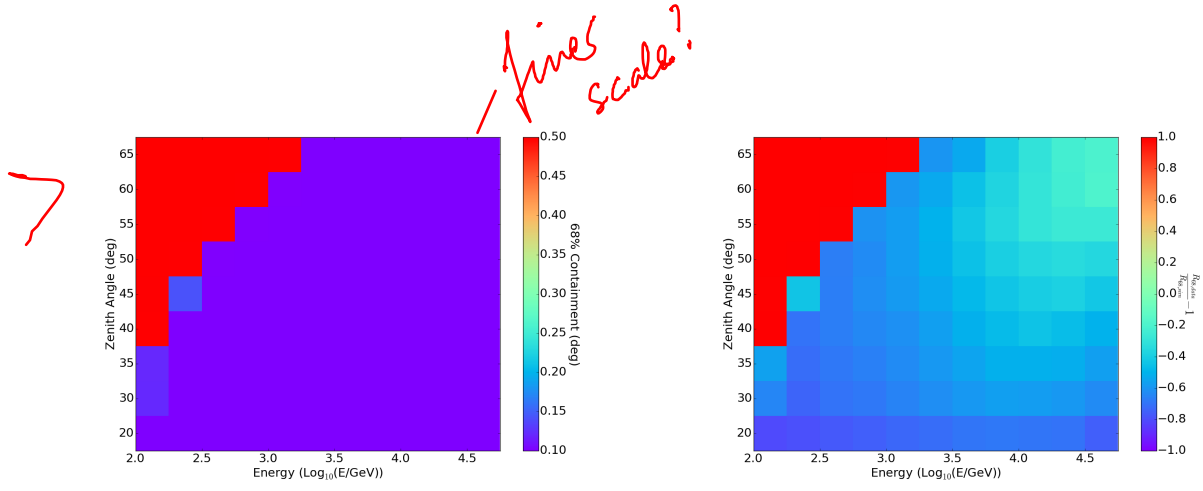
Figure 2.14: Performance of the new *Disp* method compared to Method0 and the old *Disp* method, with colors denoting the R_{68} and red denoting $\frac{R_{68, \text{new Disp}}}{R_{68, \text{old Disp}}} - 1 \geq 1$ or $\frac{R_{68, \text{new Disp}}}{R_{68, \text{reg}}} - 1 \geq 1$. The range of usefulness for Method5t (relative to Method0) now extends to $E > 1\text{TeV}$ and $\phi \geq 55^\circ$.

2.3 R_{68} for Known Objects

In order to test the validity of the results from the simulations, a known point-source with sufficient data collection at LZA and a hard spectrum (and therefore high statistics in the TeV range) was needed. Since our initial test was performed on the Crab Nebula and, in the VERITAS archival data it is the known object with the longest total exposure time at LZA, the Crab was used to generate some benchmarks. Additional objects considered for this were the Mrk421 and PKS1510-089.

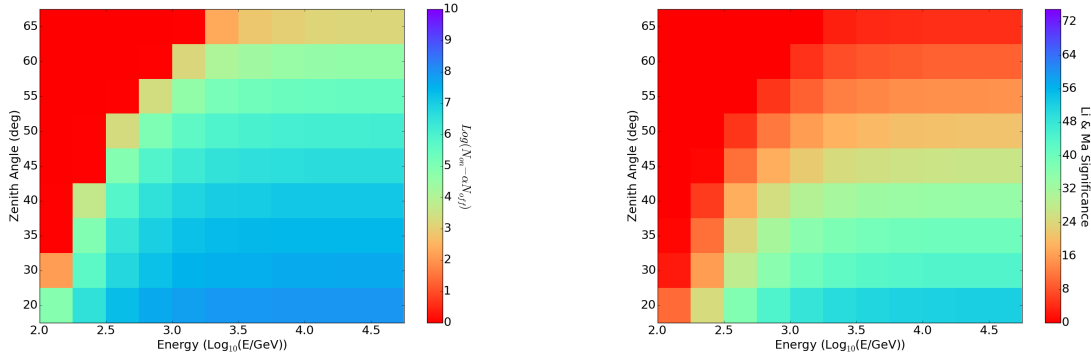
2.3.1 R_{68} for the Crab Nebula

The Crab Nebula is ~~expected~~ ^{measured} to have a GeV-TeV extension of $\sim 0.03^\circ$ [12][13]. To observe this, a R_{68} of at least 0.03° is required which, based on the simulations, we do not achieve. This however provides another metric by which to quantify our resolution, as well as to measure future gains in resolution.



(a) Angular resolution using Method5t.

(b) Deviation from simulations.

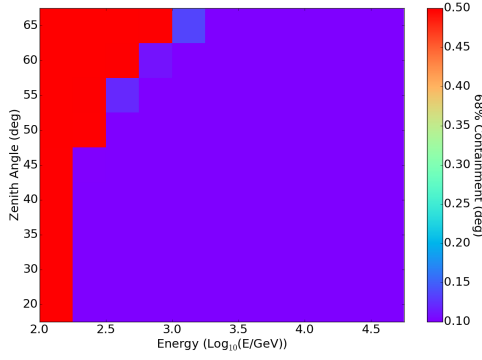


(c) Number of events ($\log(N_{on} - \alpha N_{off})$).
excess

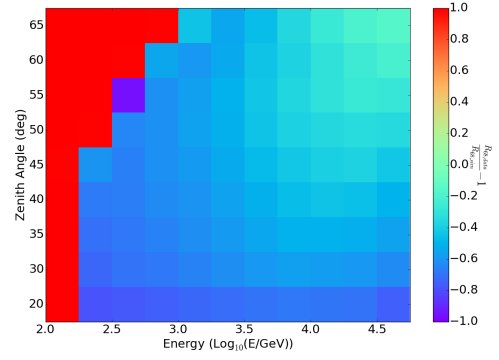
(d) Li & Ma significance.

*probably need
reference
and/or
discussion*

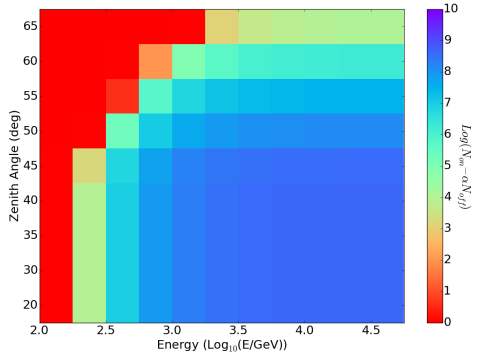
Figure 2.15: Reconstruction of the direction of the Crab Nebula horizon-to-horizon runs using the new *Disp* tables. In each case red denotes regions of no statistics.



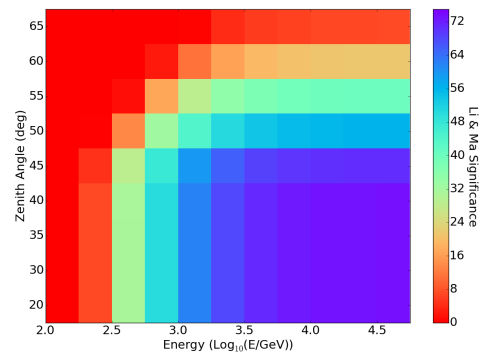
(a) Angular resolution using Method 5t.



(b) Deviation from simulations.



(c) Number of events ($\log(N_{on} - \alpha N_{off})$).



(d) Li & Ma significance.

Figure 2.16: Reconstruction of the direction of the Crab Nebula LZA runs using the new *Disp* tables. In each case red denotes regions of no statistics.

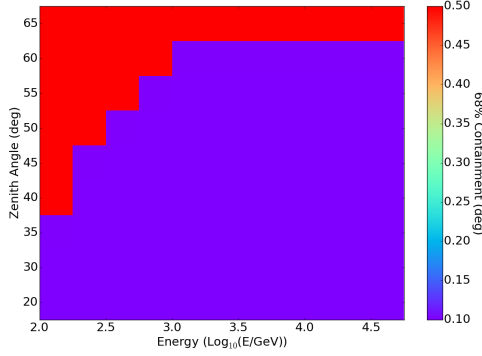
The numbers for the Crab in Fig. 2.15 suggest that we can detect the extension of the Crab.

2.3.2 R_{68} for Mrk421

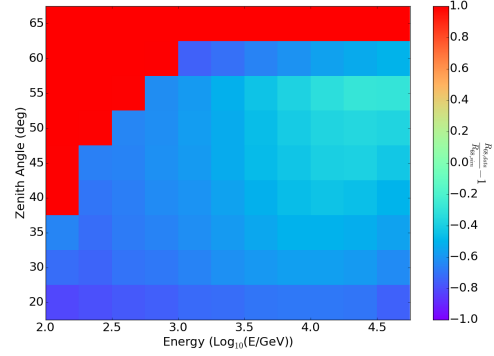
Mrk421 is an extra-galactic source ($z = 0.031$) with a hard spectrum (spectral index $\Gamma = 2.2$), but less than 5 hours of observation in the zenith range of interest ($\phi > 40^\circ$). Even with a short total duration of observation, because Mrk421 is a high-flux object, it is still

observable ^{at} high significance.

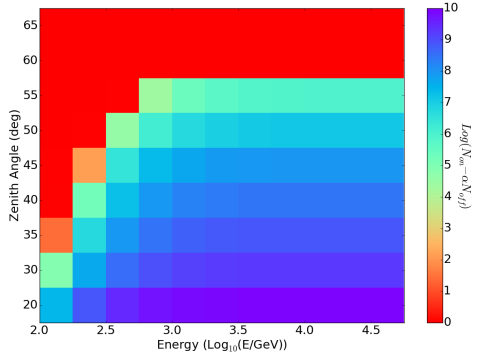
The result of this analysis was that the smallest values of R_{68} for Mrk421 ($\sim 0.08^\circ$) ^{are} found in a region of parameter space where the Li & Ma significance is negligible.



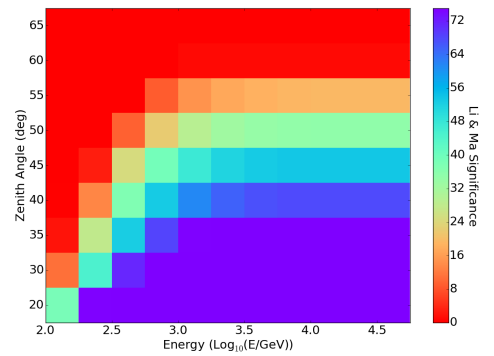
(a) Angular resolution using Method5t.



(b) Deviation from simulations.



(c) Number of events ($\log(N_{on} - \alpha N_{off})$).



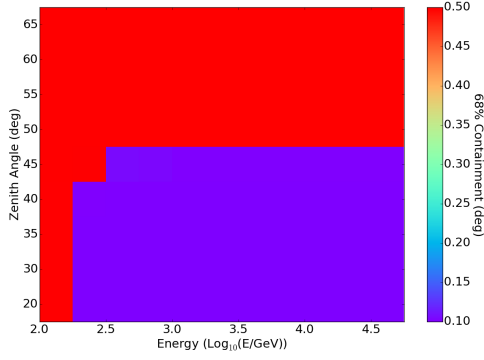
(d) Li & Ma significance.

Figure 2.17: Reconstruction of the direction of Mrk421 using the new *Disp* tables. In each case red denotes regions of no statistics.

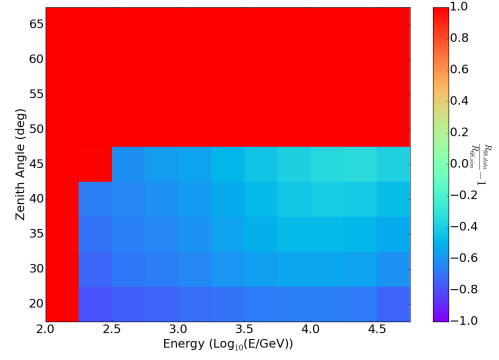
2.3.3 R_{68} for PKS1510-089

PKS1510-089 is an extra-galactic source ($z = 0.361$) with a softer spectrum (spectral index $\Gamma = 3.26$), but 17 hours of observation in the zenith range of interest ($\phi > 40^\circ$). Analysis of the data reveals that none of this falls in the region of best performance ($\phi > 45^\circ$ and

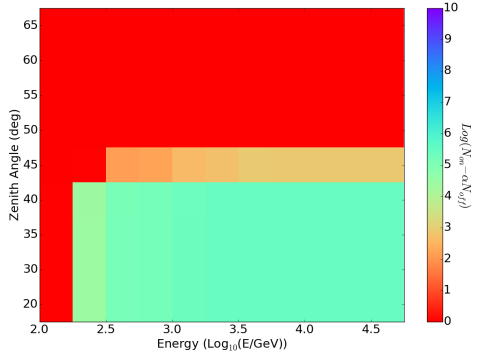
$E > 10\text{TeV}$)



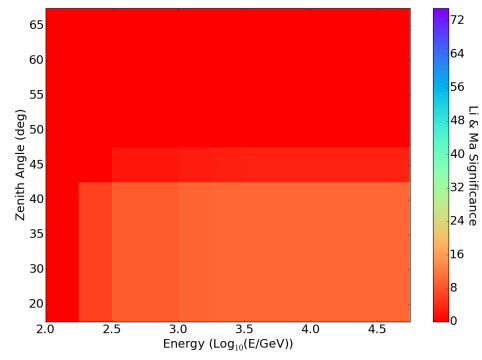
(a) Angular resolution using Method5t.



(b) Deviation from simulations.



(c) Number of events ($\log(N_{on} - \alpha N_{off})$).



(d) Li & Ma significance.

Figure 2.18: Reconstruction of the direction of PKS1510 using the new *Disp* tables. In each case red denotes regions of no statistics.

Chapter 3

Conclusions

3.1 Summary

This purpose of this work was to study and refine the *Disp* method, as well as to study the explicit and implicit dependencies of the reconstruction using this method. This revealed that:

• confirm that *Disp* is \gg better than standard at $\phi \gtrsim 45^\circ$.

- > • The 68% containment for the new *Disp* tables is at the level of 0.3° or better for energies ^{angular} above 1 TeV and zenith angles greater than 30° , and at the level of 0.2° for energies above ~ 3 TeV and zenith angles greater than 40° . At the largest zenith angles ($> 55^\circ$), this constitutes **improvements of 30-50%** (see Fig. 2.14). ✓
- > • The 68% containment is independent of noise level in the training and testing sample. ^{angular}
- > • The 68% containment is independent of the camera acceptance correction (for offset ^{angular} from the center of the camera face) used in the training.
- 3 • The 68% containment is ^{strongly} dependent on energy with the expected trend - improving ^{angular} with both energy and zenith angle up to constraints placed by low statistics.

- While the new *Disp* tables appear to perform worse than the older *Disp* tables in the SZA and MZA ranges (as measured by the 68% containment), the improvements in the LZA ranges are significant. The performance in the SZA-MZA range is not a major concern since the standard method performs as well or better in these energy ranges and requires fewer resources.
- The results obtained from an analysis of known objects are (?????) not consistent with those expected from the simulations. The reconstruction resolution determined from the Monte Carlo simulations, when tested using known source objects (Crab, Mrk 421), shows that Mrk 421 has a 68% containment of $\sim 0.08^\circ$ and that the Crab has a 68% containment of 0.08° .

3.2 Discussion

The results obtained from an analysis of known objects agree with those expected from the simulations.

3.3 Future Work

Bibliography

- [1] Nahee Park. Status of ground based gamma-ray observations. *PoS*, ICRC2017:1116, 2018.
- [2] VERITAS collaboration. VERITAS website. <https://veritas.sao.arizona.edu/>.
- [3] S. Mollerach and E. Roulet. Progress in high-energy cosmic ray physics. *Progress in Particle and Nuclear Physics*, 98:85–118, Jan 2018.
- [4] LA Antonelli, P Blasi, G Bonanno, O Catalano, S Covino, A De Angelis, B De Lotto, M Ghigo, G Ghisellini, GL Israel, et al. The next generation of cherenkov telescopes. a white paper for the italian national institute for astrophysics (inaf). *arXiv preprint arXiv:0906.4114*, 2009.
- [5] J. M. Davies and E. S. Cotton. Design of the quartermaster solar furnace. *Solar Energy*, 1:16–22, April 1957.
- [6] Dave B. Kieda. The Gamma Ray Detection sensitivity of the upgraded VERITAS Observatory. In *Proceedings, 33rd International Cosmic Ray Conference (ICRC2013): Rio de Janeiro, Brazil, July 2-9, 2013*, page 0700, 2013.
- [7] A. M. Hillas. Cerenkov light images of EAS produced by primary gamma. *International Cosmic Ray Conference*, 3, August 1985.

- [8] W. Hofmann. Data analysis techniques for stereo IACT systems. *AIP Conf. Proc.*, 515(1):318–322, 2000.
- [9] Stephane Vincent. A Monte Carlo template-based analysis for very high definition imaging atmospheric Cherenkov telescopes as applied to the VERITAS telescope array. *PoS, ICRC2015*:844, 2016.
- [10] Mathieu de Naurois and Loïc Rolland. A high performance likelihood reconstruction of γ -rays for imaging atmospheric Cherenkov telescopes. *Astroparticle Physics*, 32:231–252, Dec 2009.
- [11] HESS collaboration. H.E.S.S. website.
<https://www.mpi-hd.mpg.de/hfm/HESS/pages/home/som/2005/10/>.
- [12] M. Ackermann et al. The Search for Spatial Extension in High-latitude Sources Detected by the *Fermi* Large Area Telescope. *Astrophys. J. Suppl.*, 237(2):32, 2018.
- [13] M. Holler, D. Berge, J. Hahn, D. Khangulyan, R. D. Parsons, and H. E. S. S. Collaboration. Advanced search for the extension of unresolved TeV sources with H.E.S.S. *International Cosmic Ray Conference*, 35:676, January 2017.
- [14] Paul K. H. Yeung and Dieter Horns. The Energy-dependent γ -ray Morphology of the Crab Nebula Observed with the Fermi Large Area Telescope. *Astrophys. J.*, 875(2):123, 2019.